

Perturbative Fourier Ptychographic Microscopy for Fast Quantitative Phase Imaging

Martin Zach^{1,2,†}, Kuan-Chen Shen^{1,†}, Ruiming Cao³, Michael Unser¹, Laura Waller³,
and Jonathan Dong^{1,*}

¹Biomedical Imaging Group, École Polytechnique Fédérale de Lausanne, 1015 Lausanne, Switzerland

²Center for Biomedical Imaging, 1015 Lausanne, Switzerland

³Department of Electrical Engineering and Computer Sciences, University of California, Berkeley, CA, 94709, USA

*jonathan.dong@epfl.ch, †: Equal contribution.

January 14, 2025

Abstract

Quantitative phase imaging is a method of choice to observe structure and dynamics of unlabelled biological cells. Fourier ptychographic microscopy (FPM) reconstructs high resolution images over a wide field of view, but requires capturing many images, thus limiting acquisition speed. On the other hand, differential phase contrast (DPC) is fast but limited in resolution, as it only exploits brightfield measurements. In this study, we propose perturbative Fourier ptychographic microscopy (pFPM) as a darkfield extension of DPC for fast, high-resolution, wide-field quantitative phase imaging. We interpret DPC as a single step of the Gauss-Newton algorithm with quadratic regularization, leading to a natural generalization of multiple steps and more general regularizers. In addition, we show that phase imaging with a minimal number of illumination patterns can be achieved using the DPC brightfield illumination patterns and annular darkfield illumination patterns. Our methodology combines both a perturbative phase retrieval algorithm and annular darkfield illumination patterns.

1 Introduction

Dating back from the Zernike phase-contrast microscope [1], phase imaging has emerged as a pivotal tool to image unstained biological samples in recent years [2]. Techniques such as holography [3] or Fourier ptychography [4] retrieve quantitative phase maps via computational algorithms and have found use in many areas of biomedical research, such as histopathology or developmental biology [2, 5, 6].

The light-emitting diode (LED) array microscope, where programmable illumination enables capturing images under different illumination angles, has emerged as a versatile and rapid tool for computational phase imaging [7, 8, 9]. There, the most popular acquisition strategies are on the two ends of the speed-resolution spectrum: On the one hand, Fourier ptychographic microscopy (FPM) [4, 10] entails acquiring one image per (brightfield and darkfield) LED, typically in the range of hundreds of images. Reconstructing the high-resolution, wide field-of-view images is done with nonlinear optimization algorithms, typically gradient descent [11, 12]. On the other hand, differential phase contrast (DPC) [9, 13, 14], entails acquiring four brightfield images with asymmetric illumination patterns. There, the weak object approximation enables reconstructing the phase by solving a linear system. However, the method is only applicable to brightfield measurements, thus limiting the resolution.

When examining dynamic systems, minimizing the number of required images is paramount to achieving acceptable speed. Multiplexed Fourier ptychographic microscopy (mFPM) employs multiplexed illuminations to reduce the number of darkfield FPM images [8], combining the speed of DPC

with the high resolution of FPM. However, the nonlinear optimization becomes increasingly complex as less images are acquired, and it is unclear how to choose the illumination patterns such that the reconstruction is optimal. Learning-based methods have been suggested to address these limitations by learning optimal illumination patterns [15] or learning optimal reconstruction algorithms [16, 17, 18], improving the quality of mFPM reconstruction.

In this work, we propose a perturbative approach—perturbative Fourier ptychographic microscopy (pFPM)—for high-resolution phase imaging with a minimal number of images. From this optimization perspective, we revisit both reconstruction algorithms and illumination patterns. First, we reinterpret the weak-object approximation in DPC as the first iteration of a Gauss-Newton algorithm. Building on this, we introduce a proximal Gauss-Newton framework that includes regularization and enhances the robustness of phase retrieval reconstructions. Second, we design annular darkfield illumination patterns to perturbatively push reconstructed frequencies into the darkfield region, improving resolution. In summary, our methodology combines a perturbative reconstruction algorithm inspired by DPC with tailored illumination patterns to enable fast, high-resolution quantitative phase imaging. We validate the effectiveness of our strategy through numerical simulations and experimental results.

2 Background

2.1 LED array microscope

The resolution of a classical microscope is usually determined by the numerical aperture (NA) of the microscope objective, ν_{obj} , which sets a limit on the largest acquired spatial frequencies. The LED array microscope, where a programmable LED array replaces the illumination unit of a conventional microscope (see Fig. 1), enables capturing a wider range of frequencies by shining tilted plane wave illuminations on the object. The illumination NA, ν_{ill} , is defined as the sine of the largest tilt angle, and increases the achievable resolution to

$$\frac{1.22\lambda}{\nu_{\text{obj}} + \nu_{\text{ill}}}. \quad (1)$$

Such microscopes are typically paired with a low-NA objective to maximize the field-of-view while achieving high resolution thanks to a large illumination NA.

The LEDs are categorized depending on their position (see Fig. 1): brightfield LEDs illuminate at small angles, allowing unscattered light to be collected by the objective and producing images with high photon count and low-frequency information. Conversely, darkfield LEDs correspond to large illumination angles, generating dim images from scattered light only that contain high-frequency information.

2.2 Fourier Ptychographic Microscopy

In conventional FPM with a programmable illumination unit equipped with L LEDs, single LED illumination results in intensity measurements

$$i_l(\mathbf{r}) = |\mathcal{F}^{-1}\{p(\mathbf{k})\mathcal{F}\{o_l\}(\mathbf{k})\}(\mathbf{r})|^2, \quad (2)$$

where the LED index l ranges from 1 to L . There, $o_l(\mathbf{r}) = o(\mathbf{r}) \exp(j\mathbf{k}_l \cdot \mathbf{r})$ denotes the field resulting from illuminating the object $o(\mathbf{r})$ with an LED with associated wave vector $\mathbf{k}_l \in \mathbb{R}^2$. The intensity measurement is obtained after propagation in the microscope, characterized by a pupil function, $p(\mathbf{k})$, in Fourier space. \mathcal{F} and \mathcal{F}^{-1} denote the two-dimensional Fourier transform and its inverse, respectively, and $\mathbf{k} \in \mathbb{R}^2$ represents the 2D spatial frequency at the pupil plane. Throughout this paper, we assume an aberration-free imaging system and consequently model $p(\mathbf{k})$ as real-valued, equal to 1 inside the circular aperture and 0 outside.

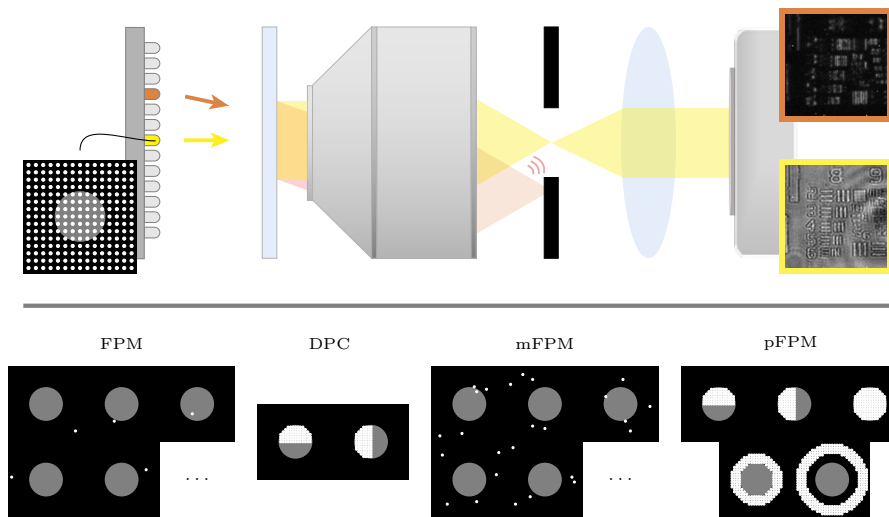


Figure 1: LED array microscope and associated illumination patterns. Top: The incident light from a programmable LED array impinges on a sample that is imaged on the camera after propagation in the microscope. The aperture (in black) determines a cut-off frequency which is directly proportional to the numerical aperture of the imaging system. The unscattered light from a brightfield LED (in yellow) is captured by the microscope, while for a darkfield LED (in orange) only scattered light is collected. Bottom: Illumination patterns for FPM, DPC, mFPM, and the proposed scheme, pFPM; the gray circle indicates the brightfield.

A variety of algorithms address the problem of recovering the object transmission function $o(\mathbf{r})$ from the intensity measurements $i_1(\mathbf{r}), i_2(\mathbf{r}), \dots, i_L(\mathbf{r})$. Since this is a nonlinear and non-convex optimization problem, gradient-based optimization is commonly employed, optionally with various acceleration strategies [11].

Successful phase reconstruction requires large overlap ratios of the pass-band of adjacent LEDs up to 0.7 [4]. This necessitates a tight LED array and consequently many, often a few hundred, measurements. This high measurement count leads to long acquisition time, limiting the temporal resolution of FPM and making it challenging to examine dynamic objects.

2.3 Multiplexed FPM

In [8], the authors demonstrate that simultaneously illuminating the object with multiple LEDs randomly chosen significantly reduces the number of measurements required to obtain similar results as FPM. In addition, the increased light throughput from multiple LEDs lowers exposure requirements. Combined, this enables the imaging of dynamic objects at high frame rates.

A set of LEDs $\mathcal{L}_m \subseteq \{1, 2, \dots, L\}$ simultaneously illuminating the object, an illumination pattern, results in intensity measurements

$$I_m(\mathbf{r}) = \sum_{l \in \mathcal{L}_m} i_l(\mathbf{r}), \quad (3)$$

i.e. the contribution of the LEDs in the illumination pattern is summed. Here, $m = 1, 2, \dots, M$ goes up to M , the number of acquired illumination patterns.

Similar to conventional FPM, researchers typically use nonlinear optimization algorithms to recover the object transmission function $o(\mathbf{r})$ from the multiplexed intensity measurements $I_1(\mathbf{r}), I_2(\mathbf{r}), \dots, I_M(\mathbf{r})$. As an example, the original publication [8] used a Gerchberg-Saxton-type algorithm. In a different line of works, researchers used data-driven algorithms for reconstruction [19, 16].

Minimizing the number of acquired illumination patterns is paramount for enabling the use of the method for imaging dynamic objects. After the initial introduction of the random patterns in [8], [16] proposes to use five illumination patterns (two brightfield patterns inspired by DPC and three annular sectors in the darkfield) in a data-driven reconstruction framework. Instead of fixing them a-priori, Kellmann et al. [20] learn illumination patterns in a data-driven framework, demonstrating successful reconstructions with single-digit number of illumination patterns.

2.4 Differential Phase Contrast

DPC¹ circumvents nonlinear optimization problems by leveraging the weak object approximation

$$o(\mathbf{r}) = \exp(-\mu(\mathbf{r}) + j\phi(\mathbf{r})) \approx 1 - \mu(\mathbf{r}) + j\phi(\mathbf{r}), \quad (4)$$

where μ is the absorption and ϕ the phase. With this approximation, the Fourier transform of the intensity measurement resulting from illumination with LED l , see Eq. (2), is

$$\mathcal{F}\{I_l\}(\mathbf{k}) = B\delta(\mathbf{k}) + h_l^{\text{abs}}(\mathbf{k})\mathcal{F}\{\mu\}(\mathbf{k}) + h_l^{\text{ph}}(\mathbf{k})\mathcal{F}\{\phi\}(\mathbf{k}), \quad (5)$$

where B is a normalization constant related to the total energy passing through the imaging system, and

$$\begin{aligned} h_l^{\text{abs}}(\mathbf{k}) &= -(\bar{p}(\mathbf{k}_l)p(\mathbf{k} + \mathbf{k}_l) + p(\mathbf{k}_l)\bar{p}(-\mathbf{k} + \mathbf{k}_l)), \\ h_l^{\text{ph}}(\mathbf{k}) &= j(\bar{p}(\mathbf{k}_l)p(\mathbf{k} + \mathbf{k}_l) - p(\mathbf{k}_l)\bar{p}(-\mathbf{k} + \mathbf{k}_l)) \end{aligned} \quad (6)$$

are the absorption- and the phase transfer function, where the overbar denotes conjugation (see [9] for a detailed derivation). Thus, under the weak-object approximation, the intensity measurements are linearly related to the phase of the object. A common simplification involves considering a phase-only sample, defined by $\mu = 0$. Multiplexed measurements can be accounted for by summing the transfer functions for the LEDs of each illumination pattern: $H_m^{\text{ph}} = \sum_{l \in \mathcal{L}_m} h_l^{\text{ph}}$. (6) suggests using asymmetric brightfield illumination patterns, resulting in full recovery of the frequencies except for the line of symmetry between illumination patterns. Thus, DPC-type reconstruction methods typically use two antisymmetric illumination patterns, where one is rotated by $\frac{\pi}{2}$ rad[16, 20].

The presence of noise in the measurements necessitates formulating the recovery problem as the regularized least-squares problem. [9] proposes L2 regularization, leading to the problem of finding

$$\min_{\phi} \sum_{m=1}^M \frac{1}{2} \|\mathcal{F}\{I_m\} - H_m^{\text{ph}}\mathcal{F}\{\phi\}\|_2^2 + \frac{\alpha}{2} \|\mathcal{F}\{\phi\}\|_2^2, \quad (7)$$

which is solved by

$$\phi(\mathbf{r}) = \mathcal{F}^{-1} \left\{ \frac{\sum_m \overline{H_m^{\text{ph}}} \mathcal{F}\{I_m\}}{\sum_m |H_m^{\text{ph}}|^2 + \alpha} \right\}(\mathbf{r}). \quad (8)$$

DPC is fast and robust, but the linear model relies on the presence of a strong unscattered wave. Consequently, it is only applicable to brightfield measurements and not darkfield images, limiting the achievable resolution to twice the objective NA. Furthermore, the weak-object approximation can be experimentally validated by comparing the brightness of brightfield and darkfield images. A substantial difference in brightness indicates a strong unscattered wave in (5), which implies that the first order terms in this equation also dominate the omitted second-order terms.

¹Nowadays, DPC is used in the context of linearized methods with asymmetric illumination patterns, as we use it here. Originally, the name stems from the computing the “differential” between intensity measurements from two mirrored asymmetric illumination patterns, canceling any influence of absorption.

3 Methods

In this section, we introduce a perturbative formalism to exploit good initial estimates and refine them. Computationally, we show that the single-shot linearization of DPC can be extended into an iterative Gauss-Newton algorithm. Experimentally, we introduce annular illuminations that take full advantage of this perturbative interpretation to refine the reconstruction using darkfield LEDs.

3.1 Discrete model

We discretize on the two-dimensional uniform Cartesian grid both the object space in $\{1, 2, \dots, d_1\} \times \{1, 2, \dots, d_2\}$ and the image space in $\{1, 2, \dots, n_1\} \times \{1, 2, \dots, n_2\}$. The discrete phase image $\mathbf{x}^* \in \mathbb{C}^D$ is of dimension $D = d_1 d_2$ and the output intensities \mathbf{y}_l are in \mathbb{R}^N with $N = n_1 n_2$. In the discrete setting, the intensity measurements (2) are modeled as

$$\mathbf{y}_l = |A_l \mathbf{x}^*|^2 \quad (9)$$

where the linear operator corresponding to the l th LED is defined as $A_l = F^* C P S_l F$, with $F : \mathbb{C}^D \rightarrow \mathbb{C}^D$ the two-dimensional discrete Fourier transform, $S_l : \mathbb{C}^D \rightarrow \mathbb{C}^D$ a circular shift in Fourier space, $C : \mathbb{C}^D \rightarrow \mathbb{C}^N$ a crop to reduce output dimension, $P : \mathbb{C}^N \rightarrow \mathbb{C}^N$ modeling the pupil function of the microscope, and finally F^* is the two-dimensional inverse discrete Fourier transform. S_l implements the phase modulation by a circular shift in Fourier space, where we round the theoretical shift determined by the LED position and the optical system to the nearest integer to avoid interpolation. Since we assume an aberration-free system, P a binary diagonal operator blanking frequencies outside of the aperture.

For multiplexed measurements, let $\mathcal{L}_1, \mathcal{L}_2, \dots, \mathcal{L}_M$ be sets of LED indices encoding the M illumination patterns, as in Section 2.3. For each $m = 1, 2, \dots, M$, the measurements are

$$\mathbf{y}_m = \sum_{l \in \mathcal{L}_m} |A_l \mathbf{x}^*|^2, \quad (10)$$

or, after letting $\mathbf{y} = (\mathbf{y}_1, \mathbf{y}_2, \dots, \mathbf{y}_M)$,

$$\mathbf{y} = G(\mathbf{x}^*), \quad (11)$$

where $G : \mathbb{C}^D \rightarrow (\mathbb{R}^N)^M$ summarizes the nonlinear multiplexed measurement acquisition. In the next section, the Fréchet derivative of G at some point \mathbf{x}^k ,

$$G'(\mathbf{x}^k) : \mathbb{C}^D \rightarrow (\mathbb{R}^N)^M : \mathbf{x} \mapsto \left(\sum_{l \in \mathcal{L}_1} \Re\{2\overline{A_l \mathbf{x}^k} \odot A_l \mathbf{x}\}, \dots, \sum_{l \in \mathcal{L}_M} \Re\{2\overline{A_l \mathbf{x}^k} \odot A_l \mathbf{x}\} \right), \quad (12)$$

will be useful, where \odot denotes elementwise multiplication.

3.2 Algorithm: Perturbative Phase Retrieval

Recovering \mathbf{x}^* from \mathbf{y} is typically posed as the least-squares phase-retrieval problem

$$\arg \min_{\mathbf{x}} \frac{1}{2} \|G(\mathbf{x}) - \mathbf{y}\|_2^2, \quad (13)$$

a nonlinear non-convex problem that is typically solved using iterative optimization algorithms. In light of the linearize-and-solve procedure of DPC, we revisit the Gauss-Newton algorithm. In the context of inverse problems, solving Eq. (13) with the Gauss-Newton algorithm is known to amplify noise in the iterates and to be extremely sensitive to the number of iterations and the initial condition, as observed by [21, 22]. To remedy this, [22] considers the regularized nonlinear least-squares problem associated with Eq. (11),

$$\arg \min_{\mathbf{x}} \frac{1}{2} \|G(\mathbf{x}) - \mathbf{y}\|_2^2 + \alpha R(\mathbf{x}), \quad (14)$$

where R is a regularization term whose influence is controlled by $\alpha > 0$. To account for nonsmooth regularizers such as total variation, [23] proposes a proximal Gauss-Newton algorithm. By approximating the nonlinear G around some point \mathbf{x}_k by $\mathbf{x} \mapsto G(\mathbf{x}_k) + G'(\mathbf{x}_k)(\mathbf{x} - \mathbf{x}_k)$, the iterations can be implemented by solving a sequence of linearized subproblems,

$$\mathbf{x}_{k+1} = \arg \min_x \frac{1}{2} \|G(\mathbf{x}_k) + G'(\mathbf{x}_k)(\mathbf{x} - \mathbf{x}_k) - \mathbf{y}\|_2^2 + \alpha R(\mathbf{x}), \quad (15)$$

see the details in Appendix A.

Revisiting the DPC algorithm from this point of view, the weak-object approximation (4) corresponds to a perturbation around the initial guess \mathbf{x}_0 constant equal to $\mathbf{1}$. Combined with a L2 (Tikhonov) regularization and a phase-only constraint, this first iteration of the Gauss-Newton algorithm yields the DPC reconstruction. In the general Gauss-Newton algorithm, we solve for a complex-valued object, and thus obtain absorption and phase information simultaneously.

Here, we consider two regularizers R : Classical L2 regularization $\mathbf{x} \mapsto \frac{1}{2} \|\mathbf{x}\|_2^2$ and isotropic total variation (TV) regularization $\mathbf{x} \mapsto \|\mathbf{D}\mathbf{x}\|_{2,1}$ where $\mathbf{D} : \mathbb{C}^D \rightarrow \mathbb{C}^{D \times 2}$ is a forward finite difference operator with Neumann boundaries and $\|\cdot\|_{2,1} : \mathbb{C}^{D \times 2} \rightarrow \mathbb{R}_+ : \mathbf{x} \mapsto \sum_{i=1}^D \sqrt{|\mathbf{x}_{i,1}|^2 + |\mathbf{x}_{i,2}|^2}$. With L2 regularization, the subproblems Eq. (15) can be solved efficiently with the conjugate gradient method [24]. For TV regularization, we solve the subproblems using the Condat-Vũ variant of the primal dual hybrid gradient algorithm [25, 26]; the details are provided in Appendix A.

In the next section, we detail an acquisition strategy that exploits the combination of DPC-type patterns with darkfield annuli to enable fast high-resolution imaging with minimal illumination patterns. However, we believe that any phase retrieval problem could benefit from the stronger noise-removal properties of the variational penalties that can be used in the proximal Gauss-Newton framework.

3.3 Acquisition strategy: perturbative FPM patterns

Based on usual DPC brightfield illumination patterns, we can reconstruct the object transmission function up to the cut-off frequency $k_{\text{BF}} = 2\nu_{\text{obj}}/\lambda$. As we aim to minimize the number of measurements, we use three brightfield illumination patterns. The first illumination pattern with all brightfield LEDs is used to obtain an amplitude image. Then, the top half-disk gives us phase information on the vertical direction and the left half-disk is its counterpart on the horizontal direction.

Following our perturbative approach, this brightfield reconstruction can be used as an initial guess for subsequent phase retrieval reconstructions with darkfield illumination patterns. We introduce annular illumination patterns to provide darkfield information with a minimal number of illumination patterns, where each concentric ring increases the region of recovered Fourier frequencies. The number of rings is tunable and allows to balance reconstruction quality with acquisition time. To double the illumination NA, results from simulations suggest that partitioning the darkfield into two rings strikes a good balance, where high-frequency details are recovered at the cost of only two additional darkfield measurements. In addition, the results show that the proposed scheme consistently provides a better reconstruction than other popular illumination patterns.

4 Results

In this section, we apply the proposed acquisition scheme and reconstruction algorithm to simulated and experimental data. In the following, DPC refers to the direct phase inversion (8) and algorithms with the suffix pFPM use multiple proximal Gauss-Newton iterations of the form (15). Methods marked with an asterisk (*) provide additional insight, but we discourage their use in practice; reasons are discussed in the respective sections. BF-pFPM* uses only the DPC illumination patterns, BF-pFPM utilizes an additional brightfield image, and DF-pFPM two additional darkfield images. For the simulations, we use L2 regularization to align with the DPC reconstruction. For the experiments, we use TV regularization to benefit from its superior noise removal properties. Details such as the number of iterations and the choice of step sizes are outlined in Appendix A.

Code and data to reproduce the results are available at <https://github.com/Biomedical-Imaging-Group/perturbative-fpm>.

4.1 Simulation

We generate the data following a generic multiplexed model as described in Section 3, with an LED array consisting of 15×15 LEDs on a regular grid spaced by 4 mm and positioned 67.5 mm from the object. We chose a numerical aperture of the objective $\nu_{\text{obj}} = 0.2$, a magnification of 10, a camera pixel size of $5.5 \mu\text{m}$, and a wavelength 514 nm. For the simulation, we illuminate LEDs up to $\nu_{\text{ill}} = 2\nu_{\text{obj}} = 0.4$, resulting in a total NA of $\nu_{\text{obj}} + \nu_{\text{ill}} = 0.6$. We generate a phase-only object with phase values in $[-0.5, 0.5]$ utilizing the `cameraman` image provided by `skimage.data`, see the details in the appendix.

Comparing DPC with BF-pFPM* in Fig. 2 demonstrates that repeating the linearize-and-solve procedure leads to better recovery of the acquired frequencies. As visible in the error map showing

$$|F\angle(\mathbf{x}^*) - F\angle(\hat{\mathbf{x}})|/|F\angle(\mathbf{x}^*)| \quad (16)$$

clamped to a maximum of 1, where \mathbf{x}^* is the reference object, $\hat{\mathbf{x}}$ is the reconstruction, and \angle is the elementwise argument of a complex vector, BF-pFPM* can recover the frequencies of the DPC pass-band almost perfectly. However, since pFPM optimizes the complex vector (as opposed to only the phase), ambiguities manifest themselves as large error along the symmetry axis between the illumination pattern. This results in oriented streaking artifacts in the reconstruction. With an additional brightfield measurement, the algorithm is able to recover frequencies up to k_{BF} completely, resulting in a satisfactory reconstruction of low frequencies. Finally, with the addition of two darkfield annuli spanning $[1, 1.5]\nu_{\text{obj}}$ and $[1.5, 2]\nu_{\text{obj}}$, high frequencies are recovered well. We discuss additional results supporting the perturbative choice of the dark field illumination in Appendix C. The qualitative results are supported by the quantitative signal-to-noise ratio (SNR)

$$10 \log_{10} \frac{\|\angle(\mathbf{x}^*)\|^2}{\|\angle(\hat{\mathbf{x}}) - \angle(\mathbf{x}^*)\|^2} \quad (17)$$

and root-mean-squared error (RMSE)

$$\sqrt{N} \|\angle(\hat{\mathbf{x}}) - \angle(\mathbf{x}^*)\| \quad (18)$$

shown in the figure.

4.2 Experimental

We apply our proposed illumination patterns and reconstruction algorithm to data acquired on a commercial inverted microscope (Nikon TE2000-U) utilizing a customized quasi-dome LED array (SCI Microscopy) [27] with a central wavelength of $0.525 \mu\text{m}$ installed on the location of the transmission illumination unit. We image the USAF-1951 phantom, a phase-only object manufactured by Benchmark Technologies, with a 10×0.25 NA objective lens (Nikon), capturing the intensity images with a sCMOS sensor (PCO Edge 5.5 monochromatic) with $6.5 \mu\text{m}$ pixels, using 50 ms and 200 ms exposure for brightfield and darkfield images respectively. We use LEDs up to $\nu_{\text{ill}} = 0.5$ for darkfield illumination, resulting in a total NA of $\nu_{\text{obj}} + \nu_{\text{ill}} = 0.75$.

Similar to the simulation results, the DPC reconstruction in Fig. 3 suffers from low-frequency artifacts, removed by BF-pFPM* at the cost of oriented streaking artifacts. The additional brightfield measurements in BF-pFPM enables satisfactory recovery of all low-frequencies without artifacts. The addition of two darkfield measurements from annuli spanning $[1, 1.5]\nu_{\text{obj}}$ and $[1.5, 2]\nu_{\text{ill}}$ enables recovery of high-frequency details, as outlined with the profile of the fifth element in group 9 shown in the inset. In contrast to the reconstructions from brightfield illumination patterns, DF-pFPM clearly resolved

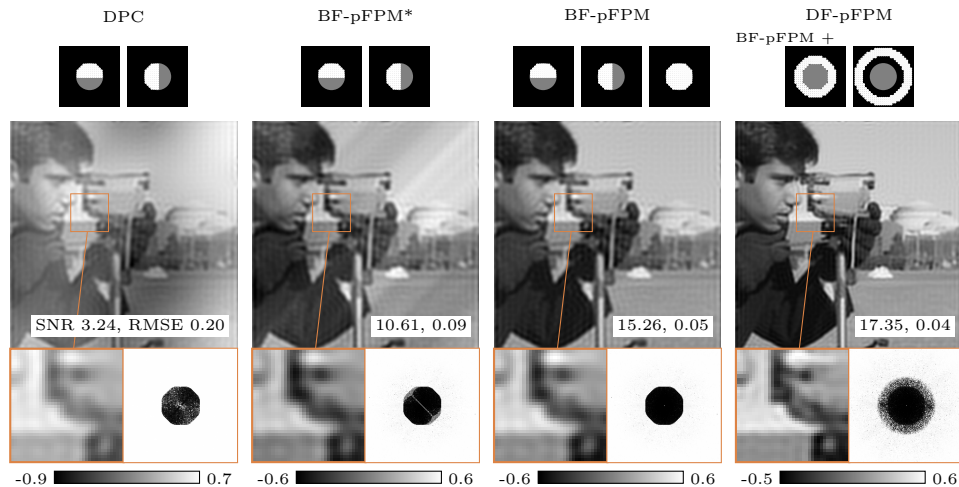


Figure 2: The DPC reconstruction only approximately recovers frequencies in the pass-band of the transfer function due to the error in the weak object approximation. BF-pFPM* almost perfectly recovers the passband region and the addition of the brightfield image enables BF-pFPM to recover all frequencies up to k_{BF} almost perfectly. With the addition of only two darkfield images, DF-pFPM recovers frequencies up to $2k_{\text{BF}}$ well.

this element, and hints also at resolving the sixth element in group 9 and even the first element in group 10. Finally, generalizing the L2 penalty used in DPC to other variational penalties proves useful, as the DF-pFPM reconstruction is almost free from high-frequency artifacts. A comparison with the reconstruction obtained by using an L2 penalty is shown in Fig. 4, discussed in Appendix B.

5 Discussion

This paper introduces a perturbative approach for phase imaging with an LED array microscope, enabling fast phase reconstruction using brightfield and darkfield LEDs with a minimal number of illumination patterns. This study encompasses both a perturbative algorithm and new darkfield illumination patterns. The two contributions can be used separately, i.e. the perturbative algorithm on other phase retrieval reconstructions and the darkfield illumination patterns with other optimization algorithms.

Building on the weak-object approximation of DPC, our approach is applicable as soon as there is a significant brightness difference between brightfield and darkfield images. The main idea behind DPC and this work is to use prior information on the object to reconstruct. This takes the form of a good initial guess to refine, which is a different approach from the regularization approach also leveraging prior information. We have demonstrated how conventional regularization such as TV improve reconstruction quality.

Deep learning regularization could provide an avenue to further improve images or decrease exposure time. More precise optical models could also be explored; for instance, the present work did not include aberrations which could be introduced in the pupil function p [28]. Furthermore, while the current work is dedicated to optical phase imaging with an LED array, it may be extended to X-ray [29] or electron microscopy [30] where DPC is also applied.

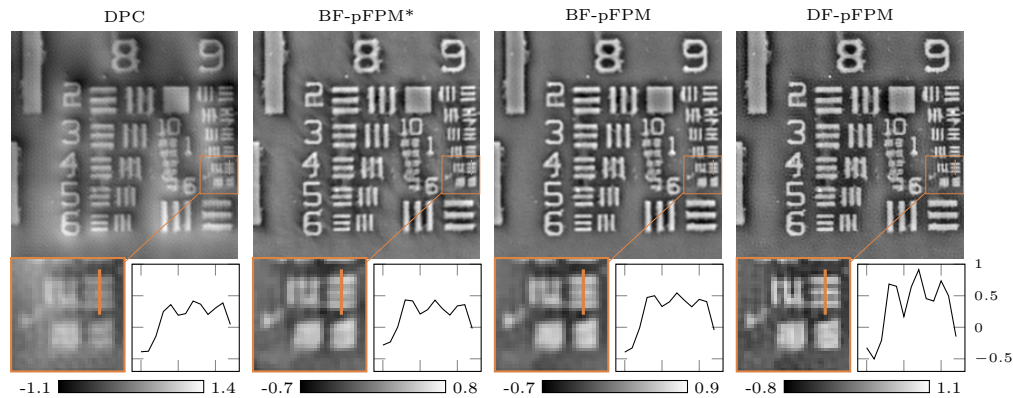


Figure 3: Phase reconstruction from measurements of the USAF-1951 phantom show low-frequency artifacts for DPC, removed by BF-pFPM* at the cost of coherent streaking artifacts due to the phase transfer function of the DPC illumination patterns. These frequencies can be recovered by an additional brightfield measurement, shown in BF-pFPM. Finally, the addition of two measurements from annuli in the darkfield provides significantly better resolution, as outlined by the line profile of the fifth element in the ninth group shown in the inset.

References

- [1] F. Zernike, “Phase contrast, a new method for the microscopic observation of transparent objects,” *Physica*, vol. 9, no. 7, pp. 686–698, 1942.
- [2] Y. Park, C. Depeursinge, and G. Popescu, “Quantitative phase imaging in biomedicine,” *Nature photonics*, vol. 12, no. 10, pp. 578–589, 2018.
- [3] D. Gabor, “A new microscopic principle,” *Nature*, vol. 161, p. 777, 1948.
- [4] G. Zheng, R. Horstmeyer, and C. Yang, “Wide-field, high-resolution fourier ptychographic microscopy,” *Nature photonics*, vol. 7, no. 9, pp. 739–745, 2013.
- [5] K. Kim, H. Yoon, M. Diez-Silva, M. Dao, R. R. Dasari, and Y. Park, “High-resolution three-dimensional imaging of red blood cells parasitized by plasmodium falciparum and in situ hemozoin crystals using optical diffraction tomography,” *Journal of biomedical optics*, vol. 19, no. 1, pp. 011005–011005, 2014.
- [6] M. Mir, T. Kim, A. Majumder, M. Xiang, R. Wang, S. C. Liu, M. U. Gillette, S. Stice, and G. Popescu, “Label-free characterization of emerging human neuronal networks,” *Scientific reports*, vol. 4, no. 1, p. 4434, 2014.
- [7] G. Zheng, C. Kolner, and C. Yang, “Microscopy refocusing and dark-field imaging by using a simple led array,” *Optics letters*, vol. 36, no. 20, pp. 3987–3989, 2011.
- [8] L. Tian, X. Li, K. Ramchandran, and L. Waller, “Multiplexed coded illumination for fourier ptychography with an led array microscope,” *Biomedical optics express*, vol. 5, no. 7, pp. 2376–2389, 2014.
- [9] L. Tian and L. Waller, “Quantitative differential phase contrast imaging in an led array microscope,” *Optics express*, vol. 23, no. 9, pp. 11394–11403, 2015.
- [10] G. Zheng, C. Shen, S. Jiang, P. Song, and C. Yang, “Concept, implementations and applications of fourier ptychography,” *Nature Reviews Physics*, vol. 3, no. 3, pp. 207–223, 2021.

- [11] L.-H. Yeh, J. Dong, J. Zhong, L. Tian, M. Chen, G. Tang, M. Soltanolkotabi, and L. Waller, “Experimental robustness of fourier ptychography phase retrieval algorithms,” *Optics express*, vol. 23, no. 26, pp. 33214–33240, 2015.
- [12] J. Dong, L. Valzania, A. Maillard, T.-a. Pham, S. Gigan, and M. Unser, “Phase retrieval: From computational imaging to machine learning: A tutorial,” *IEEE Signal Processing Magazine*, vol. 40, no. 1, pp. 45–57, 2023.
- [13] D. Hamilton and C. Sheppard, “Differential phase contrast in scanning optical microscopy,” *Journal of microscopy*, vol. 133, no. 1, pp. 27–39, 1984.
- [14] S. B. Mehta and C. J. Sheppard, “Quantitative phase-gradient imaging at high resolution with asymmetric illumination-based differential phase contrast,” *Optics letters*, vol. 34, no. 13, pp. 1924–1926, 2009.
- [15] M. Kellman, E. Bostan, M. Chen, and L. Waller, “Data-driven design for fourier ptychographic microscopy,” in *2019 IEEE International Conference on Computational Photography (ICCP)*, pp. 1–8, IEEE, 2019.
- [16] Y. Xue, S. Cheng, Y. Li, and L. Tian, “Reliable deep-learning-based phase imaging with uncertainty quantification,” *Optica*, vol. 6, pp. 618–629, May 2019.
- [17] P. Bohra, T.-a. Pham, Y. Long, J. Yoo, and M. Unser, “Dynamic fourier ptychography with deep spatiotemporal priors,” *Inverse Problems*, vol. 39, no. 6, p. 064005, 2023.
- [18] H. Wang, J. Zhu, Y. Li, Q. Yang, and L. Tian, “Neuph: scalable and generalizable neural phase retrieval with local conditional neural fields,” *Advanced Photonics Nexus*, vol. 3, no. 5, pp. 056005–056005, 2024.
- [19] J. Zhang, T. Xu, Z. Shen, Y. Qiao, and Y. Zhang, “Fourier ptychographic microscopy reconstruction with multiscale deep residual network,” *Optics express*, vol. 27, no. 6, pp. 8612–8625, 2019.
- [20] M. R. Kellman, E. Bostan, N. A. Repina, and L. Waller, “Physics-based learned design: optimized coded-illumination for quantitative phase imaging,” *IEEE Transactions on Computational Imaging*, vol. 5, no. 3, pp. 344–353, 2019.
- [21] F. Bauer and S. Kannengiesser, “An alternative approach to the image reconstruction for parallel data acquisition in mri,” *Mathematical Methods in the Applied Sciences*, vol. 30, no. 12, pp. 1437–1451, 2007.
- [22] F. Knoll, C. Clason, K. Bredies, M. Uecker, and R. Stollberger, “Parallel imaging with nonlinear reconstruction using variational penalties,” *Magnetic Resonance in Medicine*, vol. 67, no. 1, pp. 34–41, 2012.
- [23] S. Salzo and S. Villa, “Convergence analysis of a proximal gauss-newton method,” *Computational Optimization and Applications*, vol. 53, p. 557–589, Mar. 2012.
- [24] M. Hestenes and E. Stiefel, “Methods of conjugate gradients for solving linear systems,” *Journal of Research of the National Bureau of Standards*, vol. 49, p. 409, Dec. 1952.
- [25] L. Condat, “A primal–dual splitting method for convex optimization involving lipschitzian, proximable and linear composite terms,” *Journal of Optimization Theory and Applications*, vol. 158, p. 460–479, Dec. 2012.
- [26] B. C. Vũ, “A splitting algorithm for dual monotone inclusions involving cocoercive operators,” *Advances in Computational Mathematics*, vol. 38, p. 667–681, Nov. 2011.

- [27] Z. F. Phillips, R. Eckert, and L. Waller, “Quasi-dome: A self-calibrated high-na led illuminator for fourier ptychography,” in *Imaging Systems and Applications*, pp. IW4E–5, Optical Society of America, 2017.
- [28] X. Ou, G. Zheng, and C. Yang, “Embedded pupil function recovery for fourier ptychographic microscopy,” *Optics express*, vol. 22, no. 5, pp. 4960–4972, 2014.
- [29] F. Pfeiffer, T. Weitkamp, O. Bunk, and C. David, “Phase retrieval and differential phase-contrast imaging with low-brilliance x-ray sources,” *Nature physics*, vol. 2, no. 4, pp. 258–261, 2006.
- [30] N. Shibata, S. D. Findlay, Y. Kohno, H. Sawada, Y. Kondo, and Y. Ikuhara, “Differential phase-contrast microscopy at atomic resolution,” *Nature Physics*, vol. 8, no. 8, pp. 611–615, 2012.
- [31] A. Chambolle and T. Pock, “On the ergodic convergence rates of a first-order primal–dual algorithm,” *Mathematical Programming*, vol. 159, p. 253–287, Oct. 2015.
- [32] A. Chambolle, “An algorithm for total variation minimization and applications,” *Journal of Mathematical Imaging and Vision*, vol. 20, no. 1, pp. 89–97, 2004.
- [33] F. Porta, S. Villa, M. Viola, and M. Zach, “On the inexact proximal gauss–newton methods for regularized nonlinear least squares problems,” in *Advanced Techniques in Optimization for Machine Learning and Imaging* (A. Benfenati, F. Porta, T. A. Bubba, and M. Viola, eds.), (Singapore), pp. 151–165, Springer Nature Singapore, 2024.

A Details of the reconstruction algorithm

Given an iterate \mathbf{x}_k , a proximal Gauss-Newton step on the nonlinear regularized least-squares problem (14) amounts to an update rule of the form

$$\mathbf{x}_{k+1} = \text{prox}_{\alpha R}^{H(\mathbf{x}_k)} \left(\mathbf{x}_k - (H(\mathbf{x}_k))^{-1} (G'(\mathbf{x}_k))^* (G(\mathbf{x}_k) - \mathbf{y}) \right) \quad (19)$$

where $\text{prox}_{\alpha R}^{H(\mathbf{x}_k)}$ is the proximal operator of αR with respect to the metric $H(\mathbf{x}_k) = (G'(\mathbf{x}_k))^* G'(\mathbf{x}_k)$, defined as

$$\text{prox}_{\alpha R}^{H(\mathbf{x}_k)}(\mathbf{x}) = \arg \min_{\mathbf{z}} \frac{1}{2} \|\mathbf{z} - \mathbf{x}\|_{H(\mathbf{x}_k)}^2 + \alpha R(\mathbf{z}). \quad (20)$$

Proposition 6 in [23] states that (19) is equivalent to the update rule

$$\arg \min_{\mathbf{x}} \frac{1}{2} \|G(\mathbf{x}_k) + G'(\mathbf{x}_k)(\mathbf{x} - \mathbf{x}_k) - \mathbf{y}\|_2^2 + \alpha R(\mathbf{x}), \quad (21)$$

i.e. the proximal Gauss-Newton algorithm can be implemented by iteratively solving the regularized linearized problem.

For $R = \frac{1}{2} \|\cdot\|_2^2$, we solve the linear system resulting from the first order optimality condition,

$$\left((G'(\mathbf{x}_k))^* G'(\mathbf{x}_k) + \alpha I \right) \mathbf{x} = (G'(\mathbf{x}_k))^* (G'(\mathbf{x}_k) \mathbf{x}_k + \mathbf{y} - G(\mathbf{x}_k)) \quad (22)$$

using the conjugate gradient algorithm. This also covers the unregularized case by setting $\alpha = 0$. For the TV, $R = \|\mathbf{D} \cdot\|_{2,1}$, we use the dual representation of the total variation norm,

$$\alpha \|\mathbf{D} \cdot\|_{2,1} = \max_{\mathbf{z} \in \mathbb{C}^{D \times 2}} \langle \cdot, \mathbf{D}^* \mathbf{z} \rangle - \delta_{\|\cdot\|_{2,\infty} \leq \alpha}(\mathbf{z}), \quad (23)$$

where

$$\delta_{\|\cdot\|_{2,\infty} \leq \alpha}(\mathbf{z}) = \begin{cases} \infty & \text{if } \max_{i \in \{1,2,\dots,D\}} \|\mathbf{z}_i\|_2 > \alpha, \\ 0 & \text{else,} \end{cases} \quad (24)$$

and solve the nonsmooth convex-concave saddle point problem

$$\arg \min_{\mathbf{x} \in \mathbb{C}^D} \max_{\mathbf{z} \in \mathbb{C}^{D \times 2}} \frac{1}{2} \|G(\mathbf{x}_k) + G'(\mathbf{x}_k)(\mathbf{x} - \mathbf{x}_k) - \mathbf{y}\|_2^2 + \langle \mathbf{x}, \mathbf{D}^* \mathbf{z} \rangle - \delta_{\|\cdot\|_{2,\infty} \leq \alpha}(\mathbf{z}) \quad (25)$$

using the Condat-Vũ algorithm, and extension of primal-dual hybrid gradient (PDHG) with explicit gradient steps, summarized in Algorithm 1. There,

$$\mathbf{z} = \text{proj}_{\{\|\cdot\|_{2,\infty} < \alpha\}}(\bar{\mathbf{z}}) \iff \mathbf{z}_i = \frac{\bar{\mathbf{z}}_i}{\max(1, \alpha^{-1} \|\bar{\mathbf{z}}_i\|_2)} \quad (26)$$

is a pointwise projection onto the two-norm ball and at the k -th proximal Gauss-Newton (PGN) iteration, and we chose the step sizes $\tau, \sigma > 0$ as

$$\sigma = \frac{\sqrt{\|(G'(\mathbf{x}_k))^* G'(\mathbf{x}_k)\|}}{\|\mathbf{D}\|} \quad \text{and} \quad \tau = (\sigma \|\mathbf{D}\|^2 + \|(G'(\mathbf{x}_k))^* G'(\mathbf{x}_k)\|)^{-1}, \quad (27)$$

satisfying the inequality

$$\left(\frac{1}{\tau} - \|(G'(\mathbf{x}_k))^* G'(\mathbf{x}_k)\|\right) \frac{1}{\sigma} \geq \|\mathbf{D}\|^2 \quad (28)$$

needed for convergence, see [31, Remark 1]. We computed $\|(G'(\mathbf{x}_k))^* G'(\mathbf{x}_k)\|$ using 10 power iterations and used $\|\mathbf{D}\| \leq \sqrt{8}$ from [32, Theorem 3.1].

Algorithm 1: Condat-Vũ algorithm for solving Eq. (25)

Data: Number of iterations $K \in \mathbb{N}$, step sizes $\tau, \sigma > 0$, initial points $\xi_0 \in \mathbb{C}^D$, $\mathbf{z}_0 \in \mathbb{C}^{D \times 2}$

Result: ξ_K , the solution to Eq. (25)

for $k \leftarrow 0$ **to** $K - 1$ **do**

$$\left| \begin{array}{l} \xi_{k+1} = \xi_k - \tau \left(\mathbf{D}^* \mathbf{z} + (G'(\mathbf{x}_k))^* (G'(\mathbf{x}_k)(\xi_k - \mathbf{x}_k) + G(\mathbf{x}_k) - \mathbf{y}) \right) \\ \mathbf{z}_{k+1} = \text{proj}_{\{\|\cdot\|_{2,\infty} < \alpha\}}(\mathbf{z}_k + \sigma \mathbf{D}(2\xi_{k+1} - \xi_k)) \end{array} \right.$$

end

For the simulations and the experiments, we run the inner solver (conjugate gradient or Condat-Vũ) for $K = 100$ iterations from a warm-start provided by the outer Gauss-Newton iterates. Fixing the number of iterations makes this a fast, practical algorithm at the cost of an inexact solution the inner problems. The convergence of such inexact PGN methods was studied in [33]; applying their theory to the recovery problem of FPM could be subject to future work. We use 8 iterations of proximal Gauss-Newton for the simulation and the experiments, except for BF-pFPM* and BF-pFPM, where we use 4. The regularization weight α was set to 9×10^4 (L2) and 1.5×10^4 (TV) for the experiments, and 0.1 for the simulations.

B Additional reconstruction results

Figure 4 shows additional results of our reconstruction algorithm with L2 and no regularization. There, some of the results using TV regularization (in particular, BF-pFPM*, BF-pFPM, DF-pFPM) are repeated from Fig. 3 to ease comparison. In addition to the illumination patterns shown in Fig. 3, we shown reconstruction results from 3 annuli comprising LEDs in with NA in intervals $[1, 1.3]_{\nu_{\text{obj}}}$, $[1.3, 1.7]_{\nu_{\text{obj}}}$, and $[1.7, 2]_{\nu_{\text{obj}}}$ (DF-pFPM*). Similar to the simulations in Fig. 6, the improvement from increasing the number of annuli is negligible, possibly due to misalignment of the phantom while taking the images, other sources of noise, or due to the optimization parameters.

In addition to the reconstruction results from our algorithm, the image resulting from all brightfield LEDs, only the central LED, and the reconstruction from FPM data are shown in Fig. 5. The FPM reconstruction was obtained by running

$$\mathbf{x}_{k+1} = \mathbf{x}_k - \tau A^* (A\mathbf{x}_k - A\mathbf{x}_k \odot (|A\mathbf{x}_k| + \epsilon) \odot \sqrt{\mathbf{y}}) \quad (29)$$

for 50 iterations using $\tau = 1 \times 10^{-2}$ and $\epsilon = 1.5 \times 10^1$ starting from $\mathbf{x}_0 = \mathbf{1}$. This constitutes gradient descent on the ‘‘amplitude’’ loss

$$\mathbf{x} \mapsto \frac{1}{2} \| |A\mathbf{x}| - \sqrt{\mathbf{y}} \|_2^2, \quad (30)$$

which typically is preferred for FPM reconstruction [11], where $\epsilon > 0$ ensures numerical stability. Here, $A = (A_1, A_2, \dots, A_L)$ summarizes the linear operators corresponding to the individual LEDs, and the images were acquired with 1 s exposure time. The FPM reconstruction suffers from high-frequency artifacts, again possibly caused by misalignments during the image acquisition. Note that with an exposure time of one 1 s, acquiring the FPM data from 126 LEDs takes 126 s. This outlines the benefit of our approach, where acquiring the data from which the images in Fig. 3 (right) are reconstructed only takes 550 ms, reducing the chance of misalignment artifacts or inconsistent measurements due to other movements in the object, common in biological applications.

C Comparison of darkfield illumination patterns

To support the proposed annular illumination patterns, which are inspired by the perturbative principle, we compare reconstructions obtained from different illumination patterns qualitatively and quantitatively using the same simulation setup as in the main text. Fixing the number of illumination patterns to $M = 5$ and 6, we compare our illumination patterns, where three brightfield measurements are augmented by $M - 3$ annuli with equal annular radius in the darkfield, against two designs: First, the design proposed by [16] in the context of data-driven recovery, where the classical two DPC half-circles in the brightfield are augmented by annular sectors in the darkfield. However, without an additional brightfield measurement we observed the same oriented streaking artifacts as in Fig. 2. Therefore, we use the same 3 brightfield illumination patterns as for our method, and consequently partition the darkfield annulus into $M - 3$ equisized sectors. Second, a random selection similar to the selection proposed by [8] in the original publication on mFPM. There, in each illumination pattern, a fraction of $\frac{1}{M}$ of all LEDs up to ν_{ill} is activated.

The results in Fig. 6 demonstrate that the proposed annular illumination patterns consistently result in superior reconstructions as seen qualitatively in the Fourier error maps and quantitatively in the SNR and the RMSE. In addition, increasing the number of measurements from 5 to 6 gives only marginal gains, thus making the pFPM with 5 measurements a fast, practical choice for real-life applications necessitating high framerate images.

D Simulation data

We consider a region of 220×220 centered around the pixel index (200, 300) (‘‘ij’’ indexing) of the the cameraman image, \mathbf{x}^{cm} , and normalize it by

$$\mathbf{x}_{\text{norm}}^{\text{cm}} = \frac{\mathbf{x}^{\text{cm}} - \min_{i,j} \mathbf{x}_{i,j}^{\text{cm}}}{\max_{i,j} \mathbf{x}_{i,j}^{\text{cm}} - \min_{i,j} \mathbf{x}_{i,j}^{\text{cm}}} - 0.5. \quad (31)$$

Then, we generate the simulation target by encoding in the phase of a complex image, i.e.

$$\mathbf{x}^* = \exp(j\mathbf{x}_{\text{norm}}^{\text{cm}}). \quad (32)$$

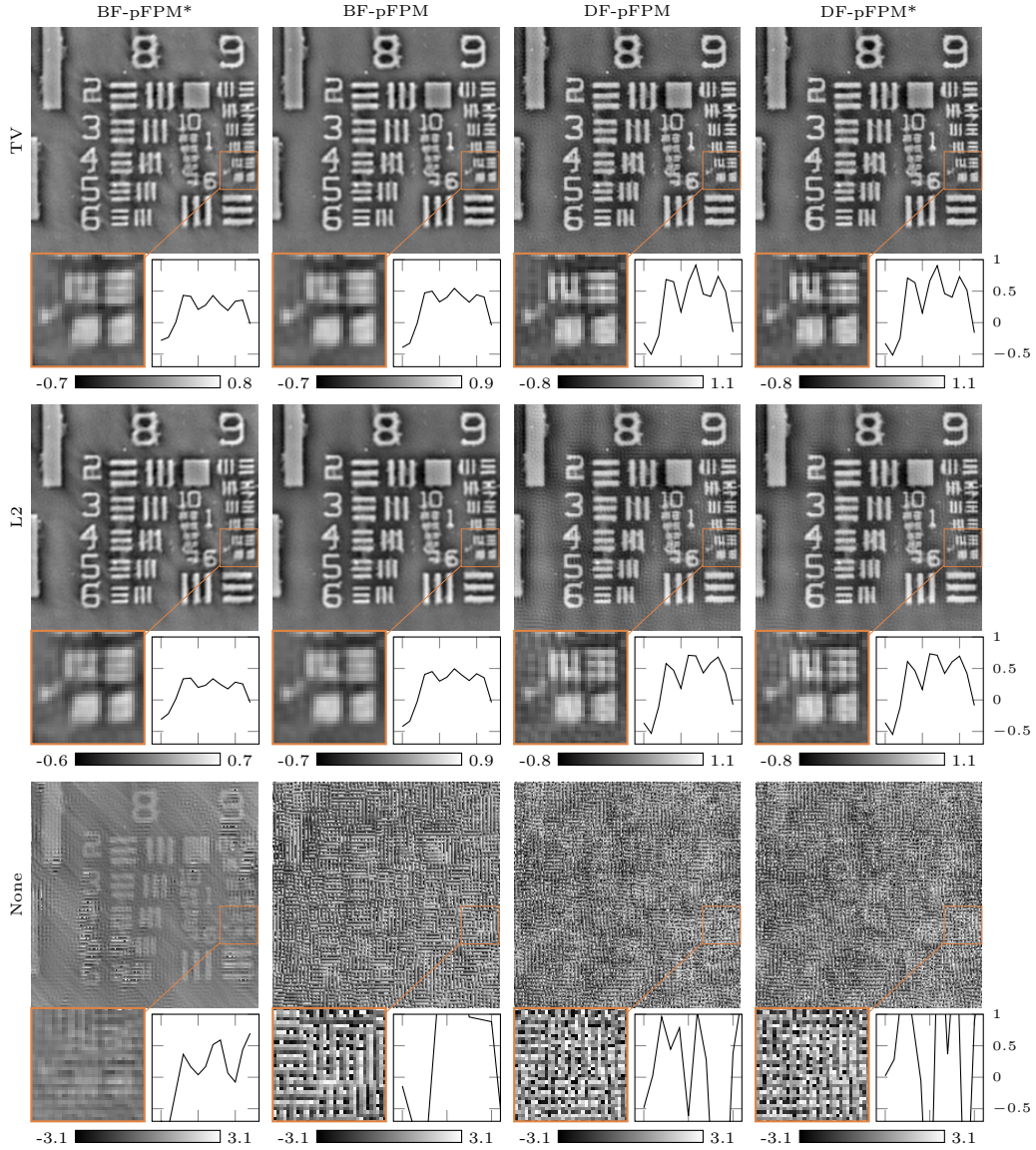


Figure 4: Effect of the regularizer in phase reconstruction from experimental data: Without regularization, high-frequency artifacts render the reconstructions useless. L2 regularization mitigates this issue, but still suffers from ringing artifacts that impede the identification of the horizontal and vertical strips of the at fifth element in group 9 of the USAF-1951 phantom. TV regularization almost entirely removes the ringing artifacts, enabling clear identification of the horizontal strips, as also shown in the line plot of the profile of phase (see Fig. 3 for the exact position of the profile).

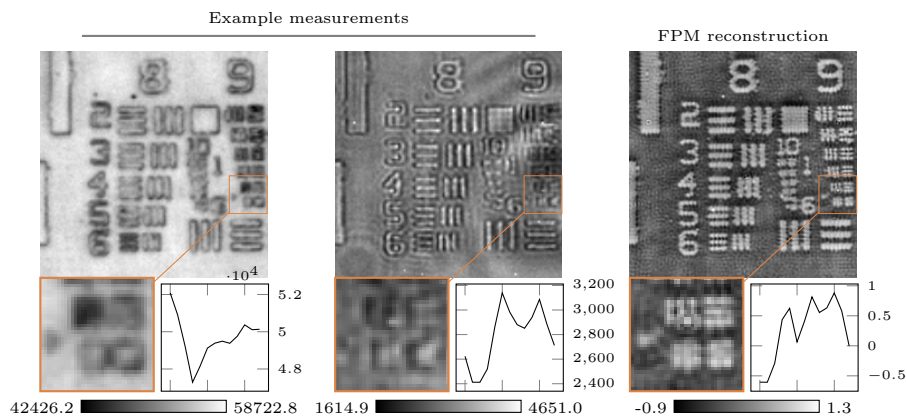


Figure 5: Left: Example measurements of the USAF-1951 phantom resulting from illumination by all brightfield LEDs (left) and by the central LED (right). Right: Reconstruction using FPM measurements. The line plot shows the profile of the fifth element in group 9 of the USAF-1951 phantom, see Fig. 3 for the exact position.

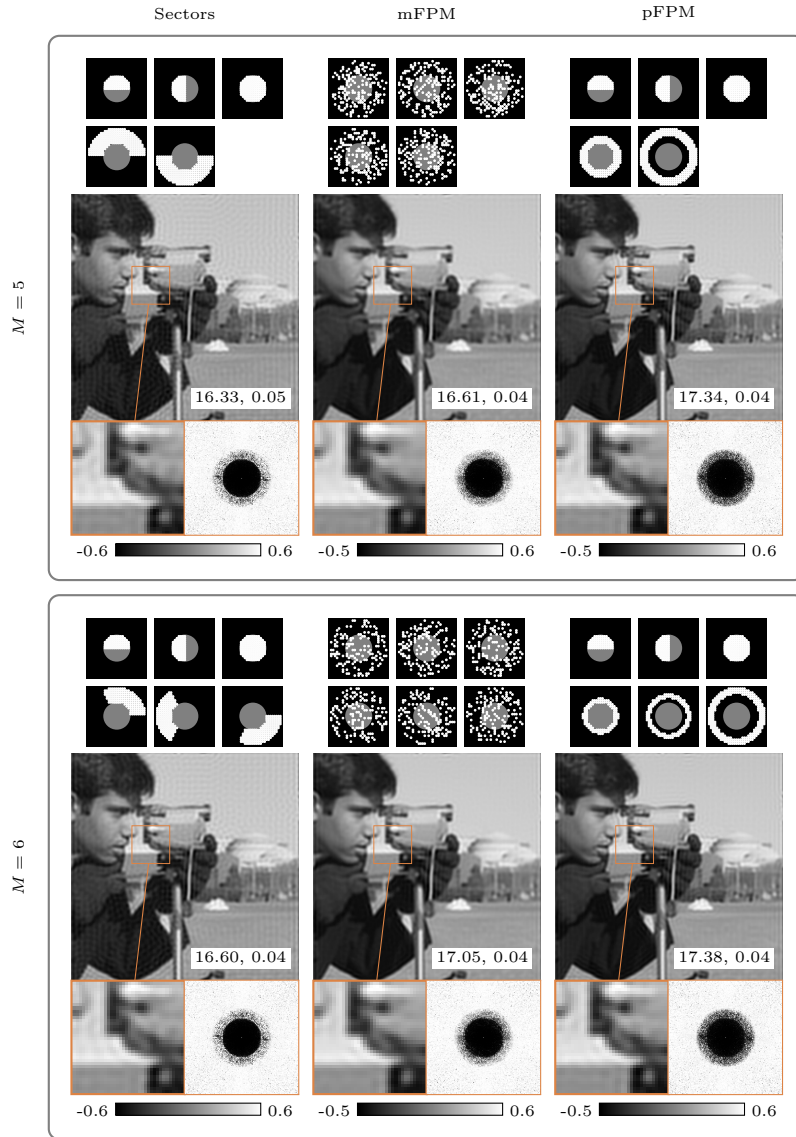


Figure 6: Comparison of different illumination patterns: When the number of illumination patterns is fixed, reconstructions from measurements using pFPM illumination pattern are consistently superior to others.